Attractive In Situ Self-Reconstructed Hierarchical Gradient Structure of Metallic Glass for High Efficiency and Remarkable Stability in Catalytic Performance

Zhe Jia[1,2], Qing Wang[1,2,4], Ligang Sun[1,2], Qi Wang[3], Lai-Chang Zhang[5], Ge Wu[1,2], Jun-Hua Luan[1,2], Zeng-Bao Jiao[6], Anding Wang[1,2], Shun-Xing Liang[5], Meng Gu[3], and Jian Lu[1,2,8]*

[1]Hong Kong Branch of National Precious Metals Material Engineering Research Center, Department of Material Science and Engineering City University of Hong Kong Hong Kong, Chin

Department of Mechanical Engineering City University of Hong Kong, Hong Kong, China

[3]Department of Materials Science and Engineering, Southern University of Science and Technology, No. 1088 Xueyuan Boulevard, Shenzhen, Guangdong 518055, China

[4]Laboratory for Microstructures, Institute of Materials Science, Shanghai University, Shanghai 200072, China

[5]School of Engineering, Edith Cowan University270 Joondalup Drive, Joondalup, Perth, WA 6027, Australia

[6]Department of Mechanical Engineering, The Hong Kong Polytechnic University, Hong Kong, China

[7]College of Science and Engineering, City University of Hong Kong, Hong Kong, China

[8]Centre for Advanced Structural Materials, City University of Hong Kong, Shenzhen Research Institute, Shenzhen 518000, China

Abstract

Metallic glass (MG), with the superiorities of unique disordered atomic structure and intrinsic chemical heterogeneity, is a new promising and competitive member in the family of environmental catalysts. However, what is at stake for MG catalysts is that their high catalytic efficiency is always accompanied by low stability and the disordered atomic configurations, as well as the structural evolution, related to catalytic performance, which raises a primary obstacle for their widespread applications. Herein, a non-noble and multicomponent $Fe_{83}Si_2B_{11}P_3C_1$ MG catalyst that presents a fascinating catalytic efficiency while maintaining remarkable stability for wastewater

remediation is developed. Results indicate that the excellent efficiency of the MG catalysts is ascribed to a unique atomic coordination that causes an electronic delocalization with an enhanced electron transfer. More importantly, the in situ selfreconstructed hierarchical gradient structure, which comprises a top porous sponge layer and a thin amorphous oxide interfacial layer encapsulating the MG surface, provides matrix protection together with high permeability and more active sites. This work uncovers a new strategy for designing high-performance non-noble metallic catalysts with respect to structural evolution and alteration of electronic properties, establishing a solid foundation in widespread catalytic applications.

1. Introduction

Metallic glasses (MGs), alternatively known as amorphous alloys or noncrystalline alloys, have always been at the cutting edge in the metals research field due to the intrinsic difference of their disordered atomic packing arrangement compared with the well-defined atomic ordering in crystalline materials.[1] Atoms with unique short-range ordered structure are randomly linked to each other, providing many fascinating possibilities owing to their atomic coordination, e.g., length of bonds, coordination numbers of metallic/metalloid atoms, electron orbital hybridization, distribution of density of electronic states, etc.[2] Moreover, the characteristic long-range disordered atomic arrangement in MGs enables their homogeneous and isotropic structure, thus greatly avoiding the structural defects in their crystalline counterparts, such as grain boundaries, stacking faults, slips, dislocations, etc.[3] In addition, several other compelling properties, e.g., their metastable nature, high Gibbs free energy, easily manipulated atomic compositions, etc., have attracted significant attention in the metallic materials research field. Largely because of their unique

structural and thermodynamic peculiarities, the MGs have exhibited many advanced structural and functional properties since their discovery, such as high strength,[4] superior elasticity,[5] excellent corrosion resistance,[6] stable wear resistance,[7] unique soft magnetic properties,[3] etc. However, due to their remaining mysterious intrinsic properties of atomic arrangement,[8] structural dynamic heterogeneity,[9] relaxation, and aging,[10] their current large-scale industrialized application has only been focused on manufacturing large-transformer units (soft magnetic property) and a few structural components such as golf drivers (elasticity and strength). Therefore, developing new practical applications of MGs is an active and pivotal topic in materials science.

Very recently, MGs have emerged as a new promising and competitive member of the family of catalysts in global environmental and energy fields. Many excellent research outcomes have demonstrated that MGs with several intrinsic catalytic advantages, such as widely tunable atomic components accompanied by fine tuning of electronic properties to satisfy catalytic selectivity demands,[11] homogeneous and isotropic characteristics affording abundant catalytic active sites,[12] the high density of unsaturated atomic coordination offering superior catalytic performance, etc.,[2] present great potential in practical catalytic applications. For example, recent reports have demonstrated that Pd–Ni–Cu–P MGs with intrinsic chemical heterogeneity and a selective dealloying function present a highly efficient and self-optimized behavior for the hydrogen evolution reaction.[12] Pt–Ni–Cu[13] and Pt–Ni–Cu–P[14] MGs, with precise regulation of surface elemental composition, exhibit highly active and durable performance in various catalytic applications. Fe–Ni–P MGs with coordinatively unsaturated Fe, Ni, and P atoms present a synergistic function in providing abundant catalytic active sites.[15] Ball-milled Fe–Si–B–Nb MG powders with high free Gibbs energy and large active sites present catalytic activity 200 times higher than their

crystalline counterparts in wastewater treatment.[16] Fe–P–C glassy ribbons with gradual formation of 3D nanopores provide enhanced electron-transfer ability during environmental catalysis.[17] In addition, in our recent reports, it was found that the production rates of the reactive transitory substances in Fe–Si–B and Fe–Si–B–Cu–Nb glassy ribbons are 5–10 times faster than the currently employed crystalline catalysts,[18,19] which is attributed to the chemical reactivity of alloys with partial crystalline phases being significantly reduced because the electrons around the randomly disordered atoms with weak atomic bonding in amorphous phase are easier to be activated.[20] However, rejuvenated catalytic behavior was observed in full crystallization owing to the electric potential differences of the generated intermetallics and grain-boundary reduction, yet the efficiency was still lower than the amorphous counterparts.[21] These results indicate that the catalytic efficiency of amorphous catalysts is indeed able to surpass that of crystalline materials. As such, this spotlights a critical issue whether the MGs can possess excellent catalytic stability while maintaining superior catalytic efficiency. However, the results of the current study demonstrate that their high catalytic efficiency is always restricted by their low stability and vice versa. For example, the addition of Nb[18] and Cr[22] into Fe–Si–B MGs could significantly enhance the catalytic stability, but at the cost of low efficiency. Herein, we report a non-noble and multifunctional MG environmental catalyst with the nominal components of $Fe_{83}Si_2B_{11}P_3C_1$ to exhibit ultrasustainable reusability over long-term cycling while maintaining superior catalytic efficiency. Such excellent performance of MG catalysts with amorphous atomic ordering can be attributed to the "self-reconstruction" capability that arises from their intrinsic isotropy and chemical heterogeneity. The self-reconstructed hierarchical gradient structure with a top porous sponge layer and a dense amorphous oxide interfacial layer encapsulating an

amorphous matrix provides self-stabilized active sites and benefits to electron transfer. The findings in this work unveil a new mechanism for MG catalysts to acquire superior durability, and more importantly, deliver a viable strategy for the design of efficient and low-cost environmental catalysts.

2. Results

2.1. Catalytic Performance

MG catalysts with an atomic component of $Fe_{83}Si_2B_{11}P_3C_1$ were manufactured by arc-melting and melt-spinning techniques in glassy-ribbon states. The amorphous nature and surface morphology of the as-received $Fe_{83}Si_2B_{11}P_3C_1$ glassy ribbon were observed by X-ray diffraction (XRD), differential scanning calorimetry (DSC), high-resolution transmission electron microscopy (HRTEM), selected area electron diffraction (SAED), and scanning electron microscopy (SEM), respectively (Figures S1 and S2, and Note S1, Supporting Information). An $Fe_{78}Si_9B_{13}$ glassy ribbon with an amorphous structure and smooth surface was also prepared for the comparison of catalytic performance (Figures S3–S5, Supporting Information). Figure 1 shows the catalytic performance of the as-received $Fe_{83}Si_2B_{11}P_3C_1$ glassy ribbons under degradation by various organic dye pollutions. As shown in Figure 1a, all the colorants including rhodamine B (RhB), methylene blue (MB), methyl orange (MO), and mixed aqueous solution with complex organic structures were progressively decolorized to colorless within 30 min using $Fe_{83}Si_2B_{11}P_3C_1$ glassy ribbons as catalysts. Nearly 100% of the color and more than 50% of the total organic carbon (TOC) can be removed within 30 min for all four different organic pollutants (Figure 1b,c). The corresponding ultraviolet visible-light (UV–vis) spectra of the four colorants' decolorization are presented in Figure S6 (Supporting Information). These results indicate that the organic

structures in the colorants are rapidly destroyed and mineralized by the generated hydroxyl radicals (OH) and sulfate radicals (SO_4^-) (Figure S7, Supporting Information) to environmentally friendly H_2O, CO_2, etc.[21] It is worth noting that the reaction system involved is not associated with any additional conditions (i.e., temperature, UV–vis irradiation, or electric fields), but only a slight addition of 2×10^{-3} m persulfate (PS) with 45 mg of $Fe_{83}Si_2B_{11}P_3C_1$ glassy ribbons, demonstrating great advances in the aspects of green, facile, low cost, and efficient wastewater remediation. Furthermore, the Fe-leached concentration (3.9 mg L^{-1}) using $Fe_{83}Si_2B_{11}P_3C_1$ glassy ribbons was much lower than the other Fe-based MGs (>10 mg L^{-1})[18] during the catalytic activity, and the leached Fe ion solution only contributed less than 5% of dye degradation, demonstrating that the dye purification in this work was primarily induced by the $Fe_{83}Si_2B_{11}P_3C_1$ glassy ribbon in heterogeneous reaction (Figure S8, Supporting Information). The effects of other experimental parameters and corresponding discussions are shown in Figure S9 and Notes S2 and S3 (Supporting Information).

Typically, the dye degradation capability of an environmental catalyst is correlated to its specific surface area and initial dye concentration with the reaction rates (kobs, which is fitted to the pseudo-first-order kinetic model, $\ln(C_0/C)=k_{obs}\,t$, where C_0 is the initial concentration of dye at t = 0 and C is the dye concentration at time t) due to the fact that the heterogeneous catalytic reaction is based on the surface reaction. Figure 1d and Table S1 (Supporting Information) present comparable results of the dye degradation ability of the $Fe_{83}Si_2B_{11}P_3C_1$ MG catalysts and other Fe-based catalysts. As shown in Figure 1d, although the crystalline zero-valence irons (ZVIs) in powders/ nanopowders form have a higher specific surface area, the Fe-based MG catalysts are still in a higher position than the ZVIs. In addition, it is noteworthy that the $Fe_{83}Si_2B_{11}P_3C_1$ glassy ribbons in this work present higher catalytic activity compared to

other Fe-based MG catalysts. Such outstanding performance is owing to the $Fe_{83}Si_2B_{11}P_3C_1$ MGs with a higher electronic delocalization state to cause stronger electron transfer capability based on lower intensity at Fermi level (E_F) in ultraviolet photoelectron spectroscopy (UPS), higher corrosion current density at the same corrosion potential in polarization curves, and smaller semicircle diameter in electrochemical impedance spectroscopy (EIS) characterizations, respectively (Figures S10 and S11a,b, Supporting Information). Moreover, the fitted equivalent circuit model indicates that the $Fe_{83}Si_2B_{11}P_3C_1$ MGs with a lower charge transfer resistance (R_{ct})of 165.0 Ω have higher electron transfer ability in the simulated dye solution compared with the $Fe_{78}Si_9B_{13}$ MGs (Figure S11c,d and Table S2, Supporting Information).[23] To further elucidate the high conductivity of the $Fe_{83}Si_2B_{11}P_3C_1$ MG catalysts, the atomic configurations and electronic structures of the MG catalysts based on first-principles simulations are shown in Figures S12 and S13 (Supporting Information). The total radial distribution function (RDF) information in Figure S12 (Supporting Information) indicates that the phosphorus (P) and carbon (C) atoms are only coordinated with iron (Fe) atoms to form Fe-P and Fe-C bonds, and no atomic coordination with silicon (Si) and boron (B) is observed. The elemental P with proper electronegativity and a medium-range atomic distance of 2.25 Å with Fe atoms is able to stabilize the Fe atoms in the amorphous state so that they have high conductivity and electron transfer ability (Figure S12, Supporting Information)[15] and that the electric potential differences among various atomic bonds can further facilitate self-activated galvanic cells.[17] In addition, it is noted that the electronic density of states (DOS) of $Fe_{83}Si_2B_{11}P_3C_1$ MGs present a flatter pattern near the EF region (Figure S13, Supporting Information), which is in good accordance with the results of UPS analysis, evidencing their stronger electronic delocalization state with higher conductivity. The adsorption energies (Eads)

and the corresponding local coordination environment of Fe sites are further studied by the simulations of combining the Adsorption Locator and Forcite programs in Materials Studio (Figure S14 and Table S3, Supporting Information). It is noted that the local adsorption sites of Fe, either containing first (E_{ads} =−51.94 kcal mol^{-1}) or second (E_{ads} =−48.63 kcal mol^{-1}) neighbor of P atoms, are more energetic for the PS adsorption compared to the adsorption sites of Fe in $Fe_{78}Si_9B_{13}$ (E_{ads} =−41.86 kcal mol^{-1}). This indicates that the addition of P atoms globally densifies the atomic packing configuration, and can further promote the presence of local Fe sites at surface. Such results further evidence that the addition of P atoms in this work plays significant effect on electron delocalization for the enhancement of catalytic performance. Activation energy (E_a) is an intrinsic kinetic characteristic of environmental catalysts for catalytic reactions and offers significant clues to explicate whether more or less energy is required to pass the catalytic reaction barrier. To calculate this value, E_a is fitted to the Arrhenius equation, $\ln k_{obs} = -E_a/R_gT + \ln A$, where k_{obs} is the kinetic rate at different temperatures (T), R_g is the gas constant, and A is a pre-exponential factor (Figure S9e, Supporting Information). As shown in Figure 1e and Table S4 (Supporting Information), the achieved E_a value of MG catalysts with various elemental components is in the range of less than 60 kJ mol^{-1} (the E_a of $Fe_{83}Si_2B_{11}P_3C_1$ MG catalysts in this work is 29.3 kJ mol^{-1}), demonstrating a much lower E_a value than the crystalline metal-based catalysts (60–250 kJ mol^{-1}).[24] From the potential-energy perspective,[25] compared to the crystals, the supercooled glassy alloys with a nonequilibrium metastable nature are always in the top position with relatively greater Gibbs' free energy, and thus they are more potentially energetic to occur the chemical reaction. The sustainability and stability of a superior catalyst is a particularly valuable attribute in environmental water remediation. Figure 1f presents the reusability of the

as-received $Fe_{83}Si_2B_{11}P_3C_1$ glassy ribbons for RhB degradation. Surprisingly, the glassy ribbons can be reused up to ≈35 times while maintaining nearly identical efficiency with the first use, following by a "tenacious" decay until reaching final shattering at≈45 reuses. The dye degradation efficiency could be sustained at nearly 80% within 20 min and at 100% within 30 min only by the addition of 2×10^{-3} m PS and use of 45 mg ribbons. Such a durable environmental catalyst with high efficiency presents great potential in practical wastewater remediation applications. To further highlight the excellent catalytic performance of the $Fe_{83}Si_2B_{11}P_3C_1$ MG catalyst, the comparable results of degradation capability versus reusability for various ion states, as well as for amorphous and crystalline Fe-based catalysts, are summarized in Figure 2, with more details presented in Table S1 (Supporting Information). The Fe ions, including ferrous (Fe^{2+}) or ferric (Fe^{3+}) ions, have been largely utilized as standard industrial Fenton-like catalysts due to their highly active homogeneous reaction. However, the ion-state Fe-based catalysts with restricted reusability (one-time usage; see bottom lefthand area of Figure 2) and the produced Fe sludge secondary pollution have gradually become a main impediment to their rapid development in industrial technologies. Comparatively, the ZVIs and Fe-based oxides with the superiorities of low cost, high efficiency, and large surface area have been reported as the iterative Fenton catalysts. However, due to the limitations of structural defects in crystals (e.g., pitting/grain-boundary corrosion, high electric resistivity owing to large grain boundaries, and fast surface decay), the reliability and efficiency of these crystalline catalysts is very constrained. As shown in Figure 2, the reported reusability of crystalline Fe-based Fenton catalysts is within 10 times. Compared with the ion-state and crystalline alternatives, the recent Fe-based MG catalysts present higher essential treating ability and more enhanced stability when degrading organic pollutants.

Surprisingly, the $Fe_{83}Si_2B_{11}P_3C_1$ glassy ribbon in this work belongs to the greatest performance group, with both ultrahigh essential treating ability and a reusability of ≈35 times without efficiency decay. Such a compelling catalytic property of the Fe-based amorphous catalysts may lead to a new, as-yet undeveloped mechanism for designing highperformance catalysts.

2.2. Structural Evolution

In order to fundamentally understand their impressive catalytic performance, structural evolution of the $Fe_{83}Si_2B_{11}P_3C_1$ MG catalysts for different numbers of reused times is carried out. The XRD patterns show that the reused $Fe_{83}Si_2B_{11}P_3C_1$ glassy ribbons are still mainly in an amorphous state even when reused up to 40 times (Figure S15, Supporting Information). Figure S16 (Supporting Information) presents the variation of surface morphology in reused glassy ribbons. Compared with the smooth surface of the as-received ribbons, many particlelike sediments are homogeneously distributed on the first-time reused ribbons followed by extensive expansion to wrinkled-like layers on the fifth-time reused ribbons. The elemental mapping results preliminarily indicate that the wrinkled layers comprise Fe oxides (Figure S16p, Supporting Information). Further increasing the reuse times, the wrinkled layers are partially dropped-off to expose the underlaid fresh layer. The surface roughness (R_q) obtained from atomic force microscopy (AFM) measurements of the first, fifth, and twentieth times reused ribbons are 17.3, 93.4, and 146 nm, respectively (Figure S17, Supporting Information). Figure 3a and Figures S18–S20 (Supporting Information) present the X-ray photoelectron spectroscopy (XPS) results for the as-received and reused glassy ribbons, respectively. Full-range XPS spectra with strong Fe 2p, Si 2p, B

1s, P 2p, C 1s, and O 1s peak intensities are observed in the MG catalysts (Figure S18, Supporting Information). Nevertheless, the S 2p peak with a weak signal is also found on the twentieth and fortieth reused ribbon surfaces due to PS adsorption and activation occurring during catalysis. As shown in Figure 3a, the metallic Fe (Fe^0) with a peak location at 707.0 eV is characterized for the as-received ribbons. After Ar^+ sputtering for a 2 nm thickness, the concentration of Fe^0 increases sharply, indicating that the Fe atoms are in zero-valence state in the as-received glassy ribbon matrix. The peaks at 710.8 and 713.8 eV demonstrate the existence of Fe^{2+} and Fe^{3+}, respectively, suggesting the formation of covalent bonding between Fe and other metalloids, which is in good accord with the simulation results in Figure S12 (Supporting Information). However, metallic Fe^0 is completely transformed to Fe^{2+} and Fe^{3+} in the reused glassy ribbons, even those that are Ar^+ sputtered (Figure S19, Supporting Information), demonstrating that the amorphous matrix with Fe^0 is the electron supplier during the catalytic performance, while further affirming the formation of Fe oxides and FeOOH. The results of XPS analysis of other elements, including O 1s in the MG catalysts, are shown in Figure S20 and discussed in Note S4 (Supporting Information). To further provide insights into the catalytic mechanism, the cross-sectional structure of the reused MG catalysts is prepared by a focused ion beam (FIB). The FIB-SEM image (Figure S21, Supporting Information) shows that the thickness of the generated wrinkled layer on the ribbon surface measures approximately 500 nm. Figure 3b displays 3D atom probe tomography (APT) images of the reused sample. It is noteworthy that the reused ribbon presents a distinct hierarchical gradient structure with Fe elements concentrated in the matrix and S/O elements mainly distributed on the top layer of the ribbon. To show the structural evolution, a spherical aberration-corrected high-angle annular dark-field scanning TEM (HAADF-STEM)

image of the cross-sectional structure is shown in Figure 3c. It is noted that the top wrinkled layer comprises a porous sponge structure with a subtop layer of super-nanometer-sized crystals (≤10 nm, Fe_2O_3 and FeOOH)[26] encapsulated in an amorphous phase with the "stem" part mainly in an amorphous structure (Figure 3d,e). With respect to the amorphous matrix area, it is worthwhile to notice that there is an approximate ≈4 nm amorphous layer with an atomic-scale short-range ordering,[27] as indicated in a combination of high resolution TEM and selected area electron diffraction images in Figure 3f,g. The corresponding atomic percentage and Fe/O ratio at different positions of the reconstructed structure is shown in Figure S22 (Supporting Information). Clearly, the reused glassy ribbon presents a gradation of Fe composition along the thickness direction, i.e., the highest Fe concentration (≈80 at%) followed by a dense amorphous layer with ≈50 at% Fe and a porous sponge layer with ≈20 at% Fe, in accord with the results of APT analysis. Figure 3h and Figure S23 (Supporting Information) show the HAADF-STEM image and the corresponding elemental distributions. Obviously, elemental Fe, Si, B, P, and C are homogeneously distributed in the amorphous matrix and elemental O and S (S is from PS, $S_2O_8^{2-}$) are concentrated on the porous sponge layer, demonstrating that the PS activation mainly occurs in the porous sponge region and the amorphous matrix is in perfect condition without being involved in the chemical reaction. When zooming the mapping results to the selected porous region (Figure S24, Supporting Information), it is found that P is more concentrated near the "skeleton," providing enhanced charge transfer due to the atomic coordination of the Fe-P bond.[15]

3. Discussion

Figure 4 shows a schematic diagram of the surface and structural variation of the $Fe_{83}Si_2B_{11}P_3C_1$ MG catalysts contributing to the catalytic reaction mechanism. During this process, the hierarchical gradient structure with the top porous sponge layer (≈500 nm) and dense amorphous thin interlayer (≈4 nm) are gradually self-reconstructed under catalytic conditions. Thanks to the intrinsic chemical heterogeneity of MGs,[2,12] the self-supported porous sponge layer with large surface area provides a stable reaction environment for charge transfer, PS adsorption, and activation for dye molecule degradation. The PS molecules rapidly go through the porous channels in the top sponge layer to arrive at the amorphous interlayer to be activated as · OH and SO_4· $^-$, which is beneficial for an effective degradation of the preadsorbed organic molecules. In addition, the generated porous sponge structure is able to avoid longdistance transmission of the radicals due to their short lifetime, i.e., a few nanoseconds.[28] Meanwhile, the elemental P concentrated near the "skeleton" with atomic coordination of an Fe-P bond can also promote the catalytic activity.[29] Notwithstanding, the densely packed, thin amorphous interlayer with superiorities of stable, excellent catalytic activity as well as high permeability to the electrons and reactants, provides promoted catalytic performance in both efficiency and sustainability.[30] The amorphous matrix with fully enriched Fe^0 plays the role of an electron "trigger" during the catalytic process. The self-activated electrons from the matrix pass the permeable amorphous interlayer easily without any obstructions (i.e., grain boundaries), providing a significant enhancement of the PS activation.

4. Conclusion

In summary, in this work we explored the $Fe_{83}Si_2B_{11}P_3C_1$ metallic glass catalysts

with disordered atomic packing structure by a facile and scalable melt-spinning technique.

The MG catalysts present excellent catalytic performance in both efficiency and stability when being used as environmental catalysts. According to the theoretical simulations, it is confirmed that the high catalytic efficiency of $Fe_{83}Si_2B_{11}P_3C_1$ MG catalysts is due to their intrinsic formation of metallic bonds and electronic delocalization with the promotion of the electron transfer that enhances the persulfate activation for the degradation of organic pollutants. Most intriguingly, owing to their selfreconstruction ability, the developed MG catalysts can be reused up to ≈35 times without obviously losing catalytic efficiency, presenting the best performance in stability and sustainability as an environmental catalyst found so far. The self-supported hierarchical gradient structure with a top porous sponge layer and an amorphous oxide interlayer provides a stable catalytic environment and highly active sites to significantly protect the under-layer amorphous matrix, which acts as an electron "trigger" during the catalytic process. In addition, this prepared $Fe_{83}Si_2B_{11}P_3C_1$ MG catalysts can be directly employed as environmental catalysts for wastewater treatment without any additional conditions (i.e., temperature, UV–vis irradiation, and electric field), demonstrating great potential in practical industrial application. The present work directly evidences a new mechanism for designing low-cost, highly efficient, and durable environmental catalysts, and more importantly, provides novel insights into the research of synthetic, non-noble catalysts in widespread catalytic application.

5. Experimental Section

Materials: The raw metals, including iron (Fe), silicon (Si), and boron (B) with a

purity higher than 99.9%, and prealloyed Fe_3P and FeC ingots were employed for metallic glass preparation. Rhodamine B, methylene blue, and methyl orange were supplied by Sigma Aldrich. Sodium persulfate ($Na_2S_2O_8$) was purchased from BDH Chemicals Ltd. (Poole, England). Tertiary butanol (TBA) and ethanol (EtOH) with a high-purity concentration of 0.5 m were used for the determination of the generated hydroxyl radicals (OH) and sulfate radicals ($SO_4\cdot^-$), respectively. Sodium thiosulfate ($Na_2S_2O_3$) was used as the quenching agent to prevent further reaction. Ferrous sulfate ($FeSO_4\cdot 7H_2O$) and ferric chloride ($FeCl_3$) were employed as homogeneous catalysts for evaluating the effect of leached Fe ions on dye degradation during the catalysis. 18.2 MΩ cm Milli-Q water was employed throughout the experiments to dilute the aqueous dye solutions. The chemicals were all of analytical grade.

Materials Preparation: MGs with the atomic components of $Fe_{83}Si_2B_{11}P_3C_1$ and $Fe_{78}Si_9B_{13}$ were prepared by our previously reported melt-spinning method (rapid solidification technique).[20] Typically, highpurity metals with designed atomic components were employed for the preparation of master alloys under a Ti-gettered Ar atmosphere by the arc-melting method. The manufactured master alloy ingots (≈20 g) were then put into a quartz crucible under a high-purity Ar atmosphere to be further melted under a temperature of 1200–1500°C. The melted alloys were then ejected onto a rotated copper roll surface with a high speed of 23–39 m s−1 following rapid quenching at room temperature. The as-quenched glassy ribbons were cut into 5 × 7 mm pieces with a thickness of 30–40 μm for the catalytic investigation conducted throughout this work. Characterization: The transmission electron microscopy (TEM), high resolution TEM (JEOL TEM 2100F FEG), scanning electron microscope (JEOL JSM-820) equipped with energy-dispersive X-ray spectroscopy (EDS), and atomic force microscope (Bruker Dimension Icon AFM) were used for the characterization of

the structural analysis and surface morphology of the as-received and reused samples. The spherical aberration–corrected high-angle annular dark-field scanning TEM images were taken with a Titan G2 60-300 electron microscope with a highly sensitive energy dispersive X-ray spectroscopy detector system. The cross-sectional structure and needle-shaped specimens of the reused glassy ribbon were prepared on an FEI Scios FIB/SEM instrument. The APT characterizations were performed in a local electrode atom probe (CAMEACA LEAP 5000 XR). The specimens were analyzed at 50 K in laser mode at a laser energy of 100 pJ, pulse rate of 200 kHz, and detection rate of 0.5%. Imago Visualization and Analysis Software (IVAS) version 3.8 was used for creating the 3D reconstructions and conducting the data analysis. X-ray diffraction (Rigaku SmartLab) with Cu Kα radiation and differential scanning calorimetry (Perkin Elmer Diamond DSC) under a purified Ar flow were used to determine the amorphous structure. The surface elemental analysis was determined by X-ray photoelectron spectroscopy equipped with Ar^+ depth-profile sputtering on a VG ESCALAB 220i-XL (the depth of Ar^+ sputtering was 2 nm in this work). The ultraviolet photoelectron spectroscopy (VG ESCALAB 220i-XL) was employed to characterize the electronic levels of the as-prepared samples. The polarization curves and electrochemical impedance spectroscopy measurements were carried out on an AutoLab PGSTAT 302N Potentiostat in the simulated aqueous dye solution (RhB concentration of 20 ppm and PS concentration of 2×10^{-3} m). The leached Fe ions were analyzed by inductively coupled plasma optical emission spectrometry (ICP-OES) (Optima 8300 ICP-OES Spectrometer, PerkinElmer) with a diluted 10 times solution using 2% w/w nitric acid (HNO_3). The dye decolorization and mineralization were assessed with a UV–vis spectrometer (Lambda2S, PerkinElmer Corp., USA) and total organic carbon measuring TOC removals (TOC-VCSH, Shimadzu), respectively.

Catalytic Properties: The catalytic performance measurements using the as-prepared glassy ribbons were carried out based on the Fentonlike reaction for RhB, MB, MO, and the mixed-dye degradation. If not specifically mentioned, each catalytic experiment involved a dye concentration of 20 ppm, catalyst dosage of 45 mg, and PS concentration of 2×10^{-3} m. The target dye solution assessments were conducted in a thermostatic water bath to adjust the constant temperature (i.e., 294.5, 303.0, 313.0, 323.0, and 333.0 K). The aqueous dye solutions (4 mL) were taken out at various time intervals of 0, 2, 5, 10, 15, 20, and 30 min followed by determination of UV–vis spectra for dye decolorization and of TOC measurements for dye mineralization. Each dye degradation experiment was conducted three times to improve experimental accuracy. The absorbance peaks (λ_{max}) of the four dyes were located at 554 nm (RhB), 664 nm (MB), 505 nm (MO), and 554 nm (mixed), respectively. For reuse experiments, each reused glassy ribbon was washed with Milli-Q water three times followed by preservation in absolute ethanol solution.

First-Principles Simulations: The structural and electronic information of $Fe_{83}Si_2B_{11}P_3C_1$ and $Fe_{78}Si_9B_{13}$ MG catalysts were calculated by ab initio molecular dynamics (AIMD) simulations by using the plane-wave[31] pseudopotential method[32] implemented in the CASTEP program[33] in Materials Studio. The exchange and correlation interactions between atoms were described by the generalized-gradient approximation.[34] The cutoff energy of the plane wave was 300 eV. The tolerance for accepting convergence of the total energy per atom was 10^{-6} eV atom^{-1}. An adequate Γ point was used to sample the Brillouin zone. The initial configurations of $Fe_{83}Si_2B_{11}P_3C_1$ and $Fe_{78}Si_9B_{13}$ containing 200 atoms in a cubic supercell with periodic boundary conditions were applied in three directions. The initial positions of the atoms were randomly assigned. All calculations were conducted under the canonical

ensemble (NVT). The temperature was controlled by the Nose-Hoover thermostat. During the simulation, the system was first kept at 2000 K for 6 ps with a time step of 3 fs to ensure the atomic structure well relaxed and artificial factors removed since this temperature was far above the melting point of the alloy. Hereafter, the system was quenched to 1000 K with a cooling rate of 2.5×10^{13} K s^{-1} and then a cooling rate of 2.0×10^{13} was employed to quench the system toward 300 K. As shown in Figure S12 (Supporting Information), the radial distribution functions of $Fe_{78}Si_9B_{13}$ is well consistent with the previous AIMD work,[35] suggesting the initial state are in amorphous structure. The splitting of the second peak indicates a typical glassy state.[36] In addition, this structure information also matches the former EXAFS results of $Fe_{79}Si_5B_{16}$.[37] Specifically, our results show that the average distances corresponding to the first peaks of Fe–Fe, Fe–B, and Fe–Si are ≈2.54, ≈2.18, and ≈2.43 Å, respectively, suggesting well concordance with the simulation and experimental results for the amorphous Fe–Si–B system. Hence, the obtained structure in our AIMD simulations is reliable for further analysis. Based on the models of as-prepared MGs derived from our AIMD simulations and constructing surface along the z-direction, the adsorption energies (E_{ads}) and the corresponding local coordination environment of Fe sites were further studied. The simulations were conducted by combining the Adsorption Locator and Forcite programs in Materials Studio. The atomic interactions were described by the universal force field,[38] combined with charge equilibration (Q_{Eq}).[39] The atomic structure of a persulfate was modeled and optimized. The geometry optimization of the MGs was also applied for the persulfate adsorption.

Supporting Information

Supporting Information is available from the Wiley Online Library or from the

author.

Acknowledgements

Z.J. and Q.W. contributed equally to this work. This work was supported by the National Key R&D Program of China (Project No. 2017YFA0204403), the Major Program of National Natural Science Foundation of China: NSFC 51590892, the RGC Hong Kong General Research Fund (Grant No. CityU 11247516), and Hong Kong Innovation and Technology Commission via the Hong Kong Branch of National Precious Metals Material Engineering Research Center (Grant No. 9448003). The TEM work was supported by the National Natural Science Foundation of China (Grant No. 21802065). The authors appreciate Dong Shen from City University of Hong Kong for the UPS measurements. J.L. designed the project; Z.J. and Q.W. conceived the experiment; Z.J., Q.W., Q.W., G.W., J.H.L., and A.W. carried out the experiments; L.S. conducted the simulations; and all authors analyzed the data and reviewed the manuscript.

Conflict of Interest

The authors declare no conflict of interest.

References

[1] a) A. L. Greer, E. Ma, MRS Bull. 2007, 32, 611; b) W. H. Wang, C. Dong, C. H. Shek, Mater. Sci. Eng., R 2004, 44, 45;

[2] Y. Pei, G. Zhou, N. Luan, B. Zong, M. Qiao, F. Tao, Chem. Soc. Rev. 2012, 41, 8140.

[3] Y. Sun, A. Concustell, A. L. Greer, Nat. Rev. Mater. 2016, 1, 16039.

[4] J. Das, M. B. Tang, K. B. Kim, R. Theissmann, F. Baier, W. H. Wang, J. Eckert, Phys. Rev. Lett. 2005, 94, 205501.

[5] B. Sarac, Y. P. Ivanov, A. Chuvilin, T. Schöberl, M. Stoica, Z. Zhang, J. Eckert, Nat. Commun. 2018, 9, 1333.

[6] P. Meagher, E. D. O'Cearbhaill, J. H. Byrne, D. J. Browne, Adv. Mater. 2016, 28, 5755.

[7] J. F. Curry, T. F. Babuska, T. A. Furnish, P. Lu, D. P. Adams, A. B. Kustas, B. L. Nation, M. T. Dugger, M. Chandross, B. G. Clark, B. L. Boyce, C. A. Schuh, N. Argibay, Adv. Mater. 2018, 30, 1802026.

[8] a) H. W. Sheng, W. K. Luo, F. M. Alamgir, J. M. Bai, E. Ma, Nature 2006, 439, 419; b) L. C. Zhang, K. B. Kim, P. Yu, W. Y. Zhang, U. Kunz, J. Eckert, J. Alloys Compd. 2007, 428, 157; c) L. C. Zhang, J. Xu, J. Non-Cryst. Solids 2004, 347, 166.

[9] Q. Wang, S. T. Zhang, Y. Yang, Y. D. Dong, C. T. Liu, J. Lu, Nat. Commun. 2015, 6, 7876.

[10] Q. Wang, J. J. Liu, Y. F. Ye, T. T. Liu, S. Wang, C. T. Liu, J. Lu, Y. Yang, Mater. Today 2017, 20, 293.

[11] N. Yang, H. Cheng, X. Liu, Q. Yun, Y. Chen, B. Li, B. Chen, Z. Zhang, X. Chen, Q. Lu, J. Huang, Y. Huang, Y. Zong, Y. Yang, L. Gu, H. Zhang, Adv. Mater. 2018, 30, 1803234.

[12] Y. C. Hu, Y. Z. Wang, R. Su, C. R. Cao, F. Li, C. W. Sun, Y. Yang, P. F. Guan, D. W. Ding, Z. L. Wang, W. H. Wang, Adv. Mater. 2016, 28, 10293.

[13] G. Doubek, R. C. Sekol, J. Li, W.-H. Ryu, F. S. Gittleson, S. Nejati, E. Moy, C. Reid, M. Carmo, M. Linardi, P. Bordeenithikasem, E. Kinser, Y. Liu, X. Tong, C. O. Osuji, J. Schroers, S. Mukherjee, A. D. Taylor, Adv. Mater. 2016, 28, 1940.

[14] M. Carmo, R. C. Sekol, S. Ding, G. Kumar, J. Schroers, A. D. Taylor, ACS

Nano 2011, 5, 2979.

[15] F. Hu, S. Zhu, S. Chen, Y. Li, L. Ma, T. Wu, Y. Zhang, C. Wang, C. Liu, X. Yang, L. Song, X. Yang, Y. Xiong, Adv. Mater. 2017, 29, 1606570.

[16] J. Q. Wang, Y. H. Liu, M. W. Chen, G. Q. Xie, D. V. Louzguine-Luzgin, A. Inoue, J. H. Perepezko, Adv. Funct. Mater. 2012, 22, 2567.

[17] Q. Wang, M. Chen, P. Lin, Z. Cui, C. Chu, B. Shen, J. Mater. Chem. A 2018, 6, 10686.

[18] Z. Jia, J. Kang, W. C. Zhang, W. M. Wang, C. Yang, H. Sun, D. Habibi, L. C. Zhang, Appl. Catal., B 2017, 204, 537.

[19] a) Z. Jia, W. C. Zhang, W. M. Wang, D. Habibi, L. C. Zhang, Appl. Catal., B 2016, 192, 46; b) S. X. Liang, Z. Jia, W.C. Zhang, X.F. Li, W.M. Wang, H.C. Lin, L. C. Zhang, Appl. Catal., B 2018, 221, 108.

[20] Z. Jia, X. Duan, P. Qin, W. C. Zhang, W. M. Wang, C. Yang, H. Sun, S. Wang, L. C. Zhang, Adv. Funct. Mater. 2017, 27, 1702258.

[21] S. X. Liang, Z. Jia, Y. J. Liu, W. C. Zhang, W. M. Wang, J. Lu, L.-C. Zhang, Adv. Mater. 2018, 30, 1802764.

[22] C. Zhang, Z. Zhu, H. Zhang, J. Phys. Chem. Solids 2017, 110, 152.

[23] P. Qin, Y. Liu, T. B. Sercombe, Y. Li, C. Zhang, C. Cao, H. Sun, L.-C. Zhang, ACS Biomater. Sci. Eng. 2018, 4, 2633.

[24] J. Chen, L. Zhu, Catal. Today 2007, 126, 463.

[25] a) P. G. Debenedetti, F. H. Stillinger, Nature 2001, 410, 259; b) F. H. Stillinger, Science 1995, 267, 1935.

[26] G. Wu, K.-C. Chan, L.-L. Zhu, L. Sun, J. Lu, Nature 2017, 545, 80.

[27] Q. Wang, C. T. Liu, Y. Yang, Y. D. Dong, J. Lu, Phys. Rev. Lett. 2011, 106, 215505.

[28] W. A. Pryor, Annu. Rev. Physiol. 1986, 48, 657.

[29] J. Kibsgaard, T. F. Jaramillo, Angew. Chem., Int. Ed. 2014, 53, 14433.

[30] W. D. Chemelewski, H.-C. Lee, J.-F. Lin, A. J. Bard, C. B. Mullins, J. Am. Chem. Soc. 2014, 136, 2843.

[31] M. D. Segall, P. J. D. Lindan, M. J. Probert, C. J. Pickard, P. J. Hasnip, S. J. Clark, M. C. Payne, J. Phys.: Condens. Matter 2002, 14, 2717.

[32] D. Vanderbilt, Phys. Rev. B 1990, 41, 7892.

[33] S. J. Clark, M. D. Segall, C. J. Pickard, P. J. Hasnip, M. J. Probert, K. Refson, M. C. Payne, Z. Kristallogr. 2005, 220, 567.

[34] Y. Wang, J. P. Perdew, Phys. Rev. B 1991, 44, 13298.

[35] J. Y. Qin, T. K. Gu, L. Yang, X. F. Bian, Appl. Phys. Lett. 2007, 90, 3.

[36] Y. Q. Cheng, E. Ma, Prog. Mater. Sci. 2011, 56, 379.

[37] Y. Takahara, N. Narita, Mater. Sci. Eng., A 2001, 315, 153.

[38] A. K. Rappe, C. J. Casewit, K. S. Colwell, W. A. Goddard, W. M. Skiff, J. Am. Chem. Soc. 1992, 114, 10024.

[39] A. K. Rappe, W. A. Goddard, J. Phys. Chem. 1991, 95, 3358.

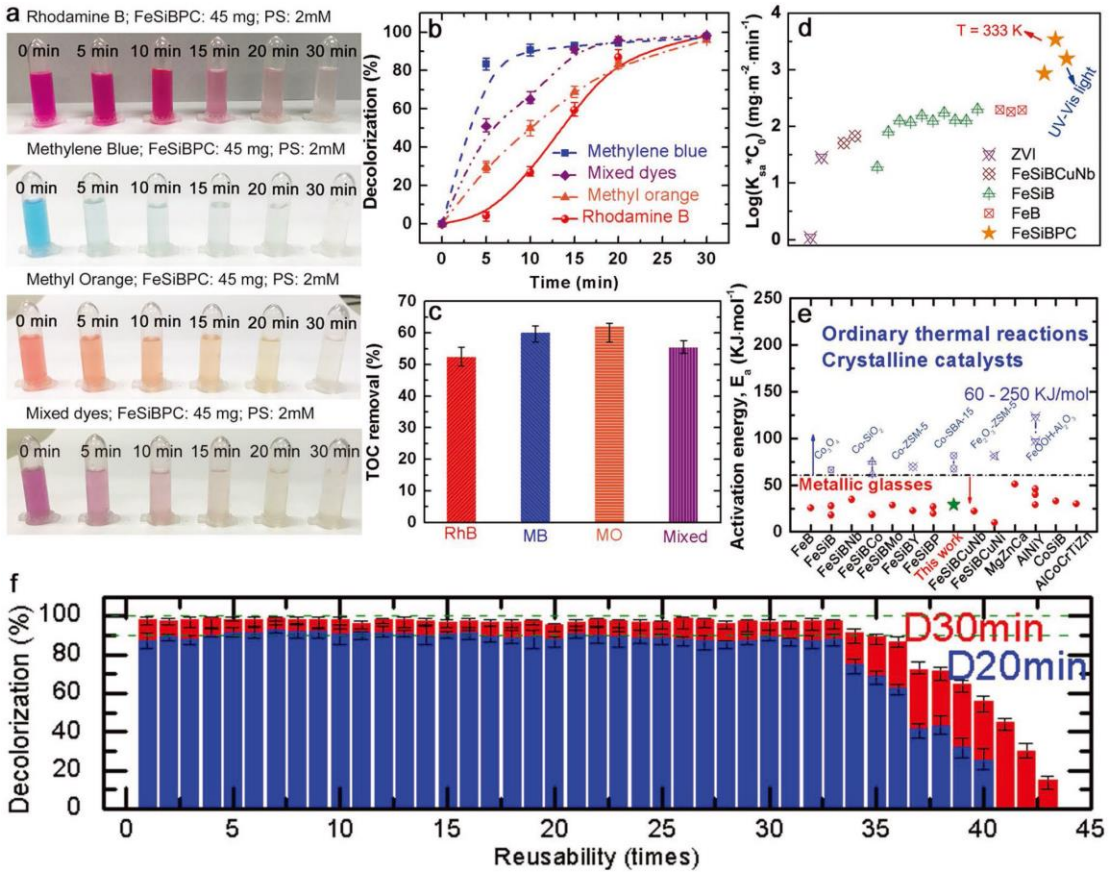

Figure 1. Catalytic performance. a) Visible color change; b) decolorization efficiency; c) TOC removal in various dye solutions using $Fe_{83}Si_2B_{11}P_3C_1$ amorphous catalysts; d) comparable results of dye degradation ability of $Fe_{83}Si_2B_{11}P_3C_1$ glassy ribbon and other Fe-based catalysts; e) comparison of activation energy (E_a) between amorphous and crystalline catalysts; f) reusability of the $Fe_{83}Si_2B_{11}P_3C_1$ glassy ribbon catalysts. (K_{sa} in (d) is the essential dye degradation ability calculated from the kinetic rate (k_{obs}) by dividing the area dosage ρ, which is calculated by $\rho = SV^{-1}$, where S and V denote the specific surface area of the catalysts and the volume of the dye solution, respectively. Additional details of (d) and (e) are presented in Tables S1 and S4 in the Supporting Information).

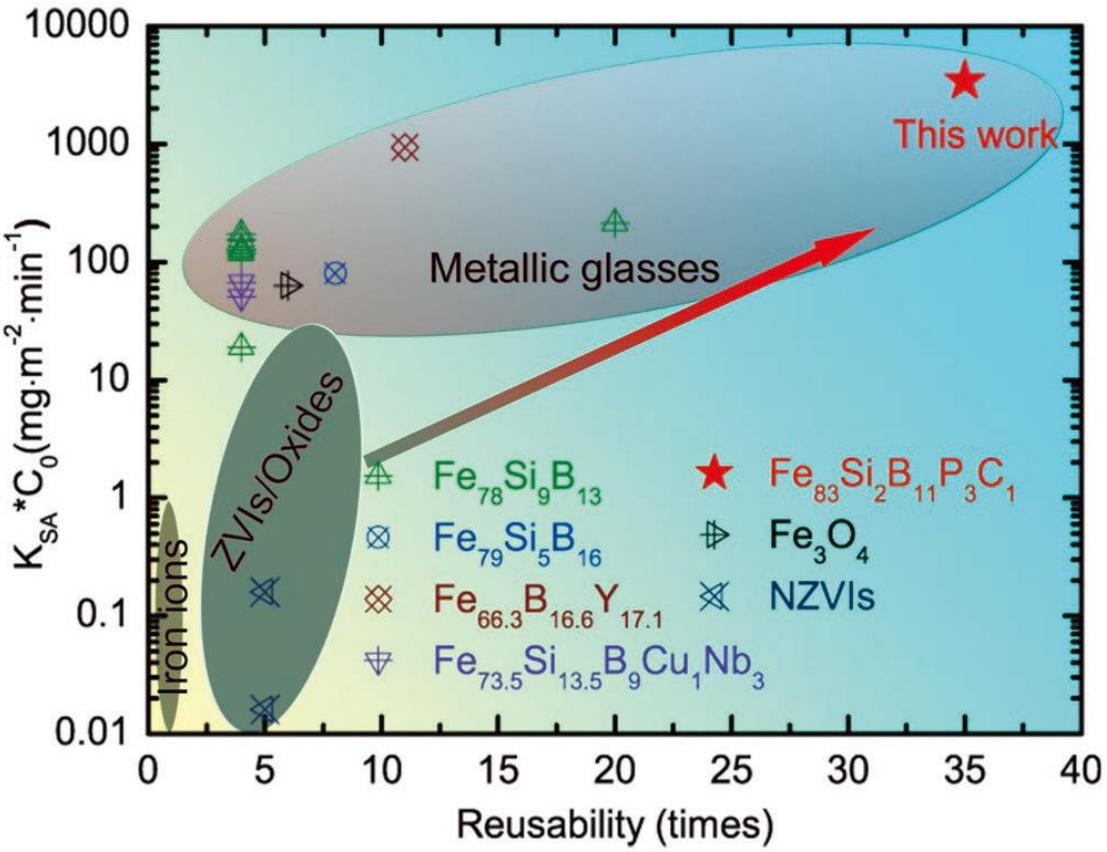

Figure 2. Comparison of catalytic performance. Degradation capability versus reusability for various amorphous and crystalline catalysts. Reusability of Fe ions is regarded as one time due to their nonreusability. An excellent catalyst should possess both high degradation efficiency and long reusability (top right-hand area) (more details are presented in Table S1 in the Supporting Information).

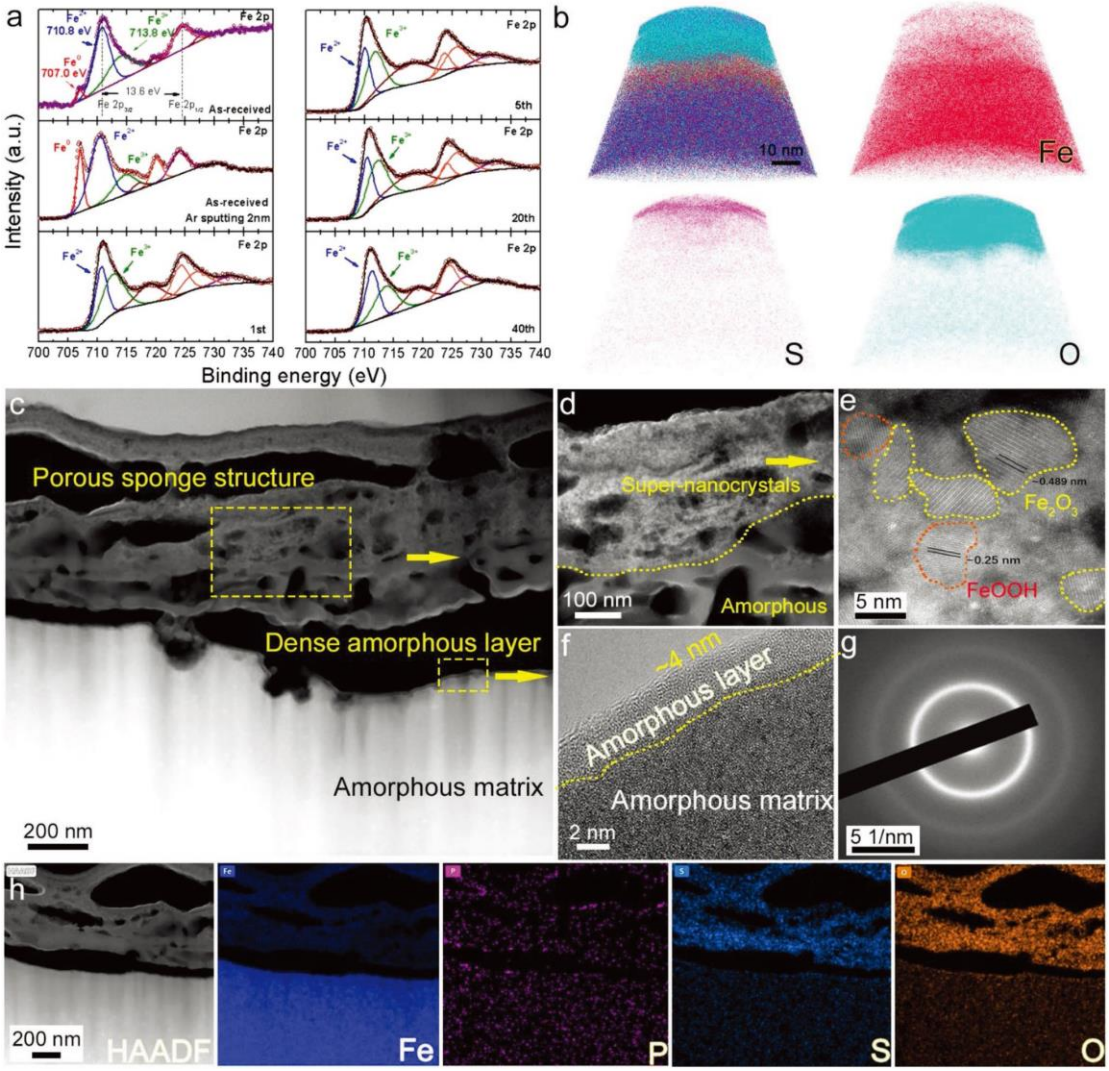

Figure 3. Structural analysis. a) High resolution XPS results of Fe 2p spectra of as-received and reused glassy ribbons. b) 3D APT images of reused ribbons. Cs-corrected STEM-HAADF images of c) the cross-sectional structure, and d,e) the zoomed selected porous sponge area in the reused glassy ribbons, showing the top glassy super-nanocrystalline structure and amorphous structure at the “stem” part. f) HRTEM image of the dense amorphous layer in (c), showing the encapsulated dense amorphous layer (thickness of ≈4 nm). g) SAED image of the amorphous matrix in (f). h) Elemental mapping results of Fe, P, S, and O.

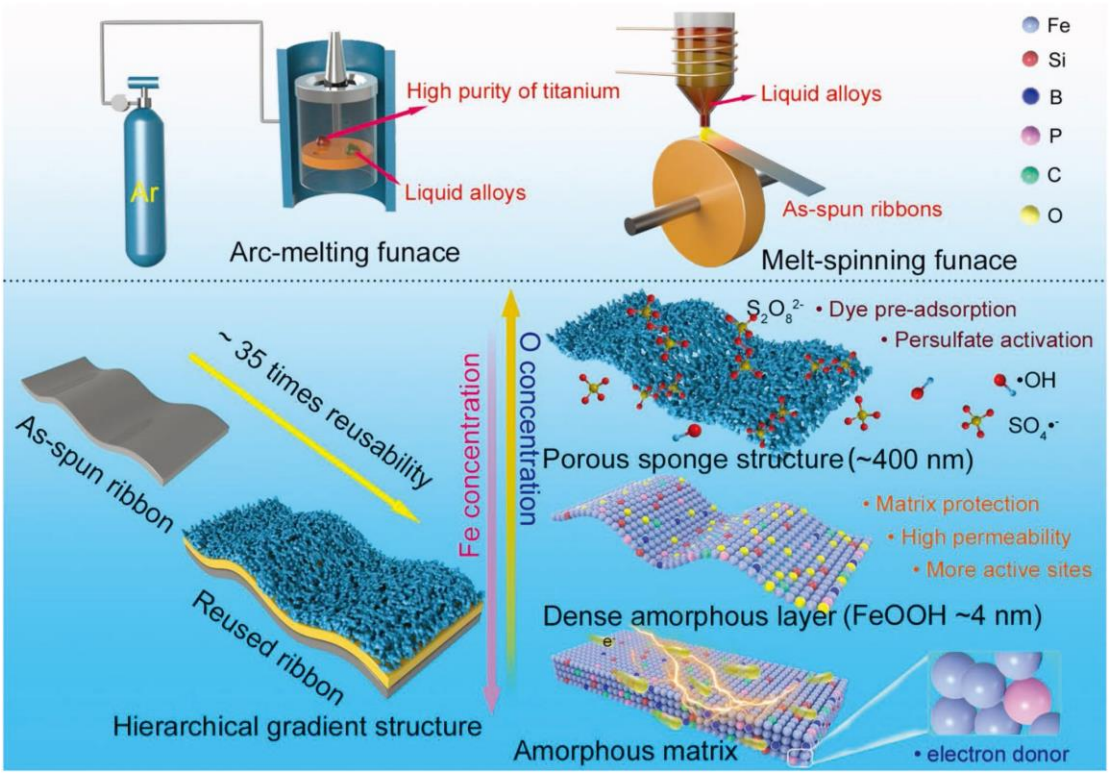

Figure 4. Schematic diagram. Surface and structural variation of as-received and reused $Fe_{83}Si_2B_{11}P_3C_1$ glassy ribbon catalysts contributing to catalytic reaction mechanism.